Synergistic factors control kinase–phosphatase organization in B-cells engaged with supported bilayers

Marcos Francisco Núñez, Kathleen Wisser, and Sarah L. Veatch*
Department of Biophysics, University of Michigan, Ann Arbor, MI 48105

ABSTRACT B-cells become activated by ligands with varying valency and mode of presentation to the B-cell receptor (BCR). We previously demonstrated that clustering the immunoglobulin M (IgM) isotype of BCR with an artificial soluble cross-linker stabilized an ordered phase-like domain that enriched kinases and depleted phosphatases to promote receptor tyrosine phosphorylation. BCR is also activated by ligands presented at surfaces, and here we activate B-cells via supported bilayers of phosphatidylcholine lipids, a natural ligand for the IgM BCR expressed in the CH27 cells used. Using superresolution fluorescence localization microscopy, along with a quantitative cross-correlation analysis, we find that BRCs engaged with bilayers sort minimal peptide markers of liquid-ordered and liquid-disordered phases, indicating that ordered-domain stabilization is a general feature of BCR clustering. The phosphatase CD45 is more strongly excluded from bilayer-engaged BRCs than a transmembrane peptide, indicating that mechanisms other than domain partitioning contribute to its organization. Experimental observations are assembled into a minimal model of receptor activation that incorporates both ordered domains and direct phosphatase exclusion mechanisms to produce a more sensitive response.

INTRODUCTION

B-cells are responsible for reacting to broad stimuli from other cells and within their environments (Youinou, 2007; LeBien and Tedder, 2008; DiLillo *et al.*, 2011). These signals can be initiated through the clustering of cell surface receptors and coreceptors by extracellular ligands and result in cellular-level responses such as the release of cytokines, processing and presentation of antigen peptides to T-cells, differentiation, clonal expansion, apoptosis, or combinations of these outcomes (Howard and Paul, 1983; Niiro and Clark, 2002;

Monroe and Dorshkind, 2007; Kurosaki *et al.*, 2009). The multisubunit B-cell receptor (BCR) combines CD79α and β signaling subunits with a transmembrane antibody that confers antigen specificity and varies in isotype during B-cell development (Reth, 1992). Signaling through BCR occurs when immunoreceptor tyrosine activation motifs (ITAM) present on CD79 are phosphorylated by the Src family kinase Lyn (Yamanashi *et al.*, 1991). Once phosphorylated, the ITAM regions become sites of docking for Lyn and other signaling mediators, such as Syk, that propagate the cellular-level immune response (Kurosaki *et al.*, 1995; Porto Dal *et al.*, 2004; Harwood and Batista, 2009).

BCR activation can occur spontaneously or be initiated when cell surface BCRs are engaged with soluble or membrane-bound antigens (Batista *et al.*, 2001). In a laboratory setting, signaling through the immunoglobulin M (IgM) isotype of the BCR is often initiated using secondary antibody fragments against the μ chain of IgM (αIgMμ) (Sieckmann *et al.*, 1978), which engage receptors away from the antigen binding site. In this case, multivalent interactions are required to cluster receptors and activate cells when soluble αIgMμ antibody fragments are used (Woodruff *et al.*, 1967; Minguet *et al.*, 2010). We recently proposed that streptavidin clustering of monomeric αIgM antibody fragments (Fab) leads to BCR activation via the stabilization of an ordered, phase-like domain that is not detectable before receptor clustering (Stone *et al.*, 2017a). This extended domain enriches Lyn kinase and depletes CD45 phosphatase to promote ITAM

tyrosine phosphorylation. These ~100 nm–diameter membrane domains, detected using superresolution fluorescence localization microscopy, resemble the liquid-ordered phase in isolated giant plasma membrane vesicles (GPMVs) in that they enrich membrane anchor peptides that contain palmitoyl groups and exclude peptides that lack palmitoyl groups (Levental *et al.*, 2010; Stone *et al.*, 2017a), albeit on smaller length scales. This proposed domain-mediated mechanism is in good agreement with extensive past investigations using detergent extraction, cholesterol depletion, and Förster resonant energy transfer (FRET; Yamanashi *et al.*, 1991; Cheng *et al.*, 1999; Sohn *et al.*, 2006, 2008) in which BCR activation is attributed to clustered BCR residing within ordered domains, sometimes referred to as lipid rafts (Simons and Ikonen, 1997, Lingwood and Simons, 2010). The major distinction between our proposed mechanism and previous models is that past models posited that BCR altered its domain partitioning into existing rafts upon clustering (Cheng *et al.*, 2001; Pierce, 2002). We propose that the act of clustering BCR itself stabilizes existing ordered domains without an inherent change in BCR domain preference (Stone *et al.*, 2017a).

Cellular responses mediated through the BCR are often more reactive when cells engage with natural ligands (Volkmann *et al.*, 2016) or when antibodies or ligands are presented on surfaces (Carrasco *et al.*, 2004), where monovalent binding to receptors is sufficient to activate cells (Tolar *et al.*, 2009a). This could arise from surface-mediated adhesion forces that can cluster receptors and exclude bulky components from sites of receptor engagement even in the absence of multivalent interactions in simple systems (Albersdorfer *et al.*, 1997; Sackmann and Smith, 2014). More specifically to B-cells, past work demonstrates that BCRs contain structural domains that enhance self-clustering specifically upon surface engagement (Tolar *et al.*, 2009a,b) and that actin-driven forces promote domain coarsening when receptors engage with mobile, bilayer-supported ligands (Fleire *et al.*, 2006; Rey-Suarez *et al.*, 2020). It is also suggested that surface engagement of BCR can lead to enhanced receptor activation via the local depletion of transmembrane phosphatases with bulky ectodomains (Harwood and Batista, 2009), analogous to effects directly demonstrated in other immune-receptor signaling systems (Choudhuri *et al.*, 2005; Freeman *et al.*, 2016; Schmid *et al.*, 2016; Carbone *et al.*, 2017; Bakalar *et al.*, 2018).

In this study, we demonstrate that ordered, phase-like domains are stabilized by BRCs engaged with bilayer-presented ligands, and we explore how membrane domains work in concert with other organizing principles to facilitate receptor activation under this stimulation condition. This is accomplished using multicolor superresolution fluorescence localization imaging (Betzig *et al.*, 2006, Hess *et al.*, 2006, Rust *et al.*, 2006) combined with a quantitative cross-correlation analysis (Sengupta *et al.*, 2011, Veatch *et al.*, 2012), which has the resolution and sensitivity to detect subtle, domain-mediated interactions in intact cells. Our experimental findings motivate a refinement to the minimal predictive model for BCR activation developed previously to describe responses to soluble cross-linkers (Stone *et al.*, 2017a). We include an additional repulsion for down-regulating phosphatases that synergizes with phase-like domains to enhance both antigen sensitivity and the magnitude of receptor activation.

RESULTS

Phosphatidylcholine lipids incorporated into supported lipid bilayers are a natural ligand for CH27 B-cells

The CH27 cells used in this study express an IgM isotype of the BCR, and past work indicates that this BCR is activated upon specific engagement with phosphatidylcholine (PC) lipids adsorbed onto

soluble proteins, intact red blood cells, or liposomes (Haughton *et al.*, 1986; Mercolino *et al.*, 1986). This sensitivity was verified by probing calcium mobilization and BCR phosphorylation state, two indicators of BCR activation, and results are summarized in Figure 1.

Changes in cytoplasmic calcium levels in response to PC lipids were monitored using the cytoplasmic calcium indicator Fluo-4, whose fluorescence intensity increases when it is bound to Ca^{2+}, providing a measure of cytoplasmic Ca^{2+} concentration. Cells were deposited onto a glass-bottom dish with a planar supported lipid bilayer (PLB) and allowed to settle over time while Fluo-4 intensity was monitored by fluorescence microscopy (Figure 1A). An increase
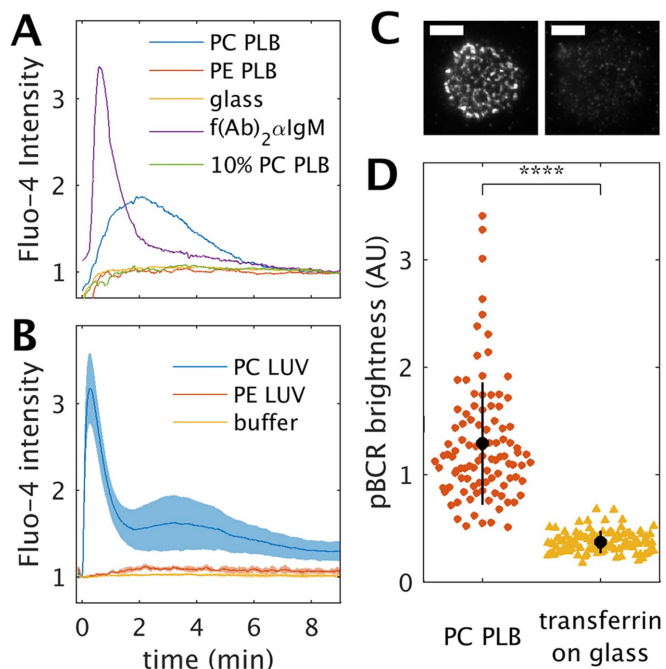

FIGURE 1: CH27 B-cells activate robustly through their BCR upon engagement with PC lipid-containing membranes. (A) Calcium mobilization is detected using the cytoplasmic calcium indicator Fluo-4 in CH27 cells deposited onto planar lipid bilayers (PLBs) of POPC lipids or when cells supported on glass are incubated with dimeric f(Ab)2 against IgMμ, but not when cells settle on glass or a membrane containing only 10% POPC. Here the average Fluo-4 level across a field of cells is plotted vs. time after cells are introduced into the chamber and levels are normalized to the value at long stimulation times (9 min). Traces in figures are from single experiments but are representative of results obtained over at least three independent measurements. (B) Calcium mobilization is also detected in CH27 cells probed in suspension upon exposure to large unilamellar vesicles (LUVs) of POPC but not appreciably in cells exposed to LUVs of POPE or a buffer control. Traces shown represent the average values of normalized curves over at least three independent measurements and shaded regions represent the SD between measurements. (C) Staining of CH27 cells using an antibody against phosphorylated BCR (pBCR) imaged under total internal reflection indicates that BCR is phosphorylated in cells engaged with PC membranes compared with an unstimulated control conjugated to a glass surface through biotinylated transferrin (top right). Images are acquired under the same illumination conditions and displayed the same intensity scale. All scale bars are 5 μm. (D) The quantification shows the average brightness across the cell footprint over >100 individual cells for the conditions shown. Quantification derives from one measurement that was representative of three independent measurements. Significance was determined using a two-sample *t* test (ttest2 in Matlab), where **** indicates that $p < 0.0001$.

in Fluo-4 intensity was observed when cells settled onto a supported lipid bilayer of PC lipids, indicating that cells mobilize calcium under this stimulation condition. As a positive control, cells adhered to a glass slide were incubated with dimeric soluble antibody fragments (f(Ab)₂) against IgMμ (αIgM). These cells stimulate synchronously, leading to a coherent and therefore larger initial response averaged over all cells. Calcium mobilization was not observed when cells settled onto membranes with low PC content or membranes made exclusively of phosphatidylethanolamine (PE) lipids, or when cells settled directly onto a clean glass coverslip. We additionally probed the calcium response for cells in suspension incubated with 100 nm–diameter large unilamellar vesicles (LUVs) via a plate reader fluorimeter assay (Figure 1B). Here we found that calcium mobilization occurs when CH27 cells are incubated with POPC LUVs, but not appreciably when cells are incubated with POPE LUVs.

The BCR phosphorylation state was assayed by antibody against the CD79α (Igα) subunit of the BCR phosphorylated at Tyr-182 (pBCR). Cells chemically fixed and stained 5 min after coming into contact with a PC lipid bilayer exhibit punctate pBCR staining when imaged in total internal reflection (TIR), indicating that a pool of BCR is activated upon engagement with the PC lipid membrane, but not in control cells that are adhered to glass presenting streptavidin via biotinylated transferrin (Figure 1C). pBCR staining indicates that activated BCRs are organized to extended, sometimes noncircular domains at the cell surface, in agreement with previous studies (Carrasco et al., 2004; Carrasco and Batista, 2006; Fleire et al., 2006). Figure 1D shows a quantification of the average pBCR brightness across multiple cells. Together, these measurements support past observations that CH27 cells are activated specifically by PC lipid headgroups and that activation occurs through engagement of BCR.

Markers of ordered and disordered phases sort with respect to BRCs engaged with phosphatidylcholine lipid membranes

We next monitored the sorting of two mEos3.2 conjugated minimal peptides with respect to clusters of phosphorylated BCR in CH27 cells in contact with PC lipid bilayers using superresolution fluorescence localization microscopy (Figure 2). The PM peptide is the palmitoylated and myristoylated anchor sequence from Lyn that partitions with the liquid ordered (Lo) phase in giant plasma membrane vesicles (GPMVs) (Pyenta et al., 2001; Stone et al., 2017a), while the TM peptide is the transmembrane helix from LAT with mutations at palmitoylated cysteines that partitions with the liquid-disordered (Ld) phase in GPMVs (Levental et al., 2010; Lorent et al., 2017; Stone et al., 2017a). Amino acid sequences of these probes and their posttranslational modifications are shown in Supplemental Figure 1. In past work, we found that these peptides sorted differentially with respect to BRCs in CH27 cells formed by cross-linking biotinylated Fab αIgM with soluble streptavidin. Here we ask whether a similar trend is observed when BCR is engaged with PC bilayers.

CH27 cells transiently expressing either PM or TM peptides conjugated to the photoactivatable probe mEos3.2 were introduced onto glass-supported PC planar bilayers within simple flow chambers at room temperature as described in *Materials and Methods*. The use of a flow chamber reduces the time required for cells to settle onto the bilayer surface, enabling us to probe the relatively short activation time (5 min) for comparison with previous work (Stone et al., 2017a). After being incubated for 5 min, cells were chemically fixed; then pBCR was labeled with primary antibody (CD79α Tyr182), and visualized with an
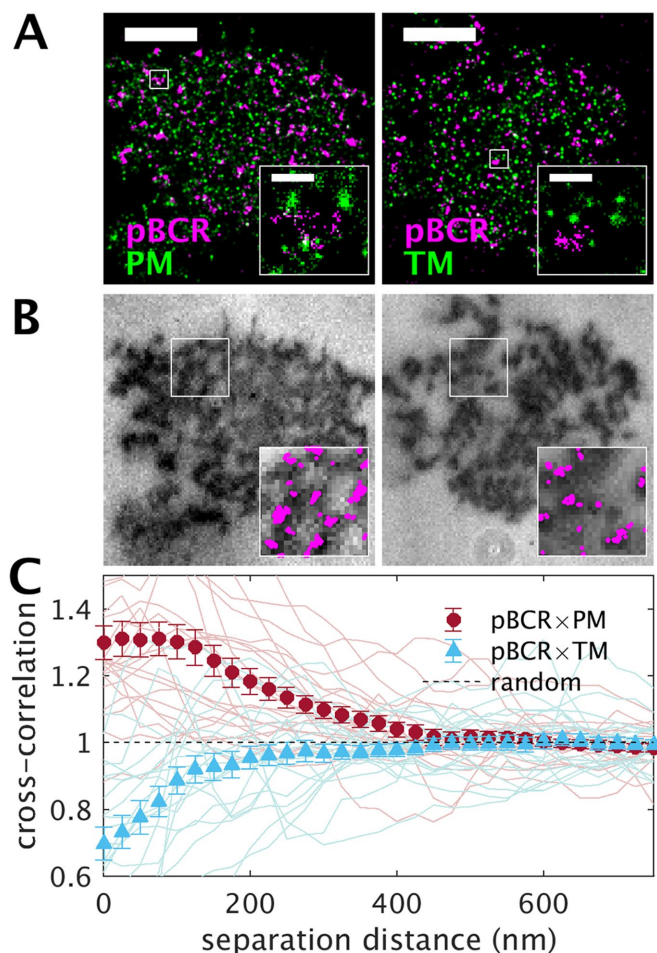

FIGURE 2: Phase-marking minimal peptides sort with respect to BRCs formed through engagement-supported bilayers of POPC. (A) Representative reconstructed superresolution images of pBCR antibody stained with Atto655 and the minimal membrane-anchored peptides PM (left) or TM (right) conjugated to mEos3.2. Scale bars are 5 μm in main images and 500 nm in insets. (B) ICM images report on the distance between the plasma membrane and the glass support and indicate that these cells exhibit significant membrane topography across the basal cell surface. Insets show colocalization of dark areas in the ICM image and pBCR localizations (magenta) from part A. (C) Cross-correlation functions tabulated for 20 cells between pBCR and PM or 20 cells between pBCR and TM from images acquired from at least three distinct sample preparations. Curves from individual cells are shown as lighter color lines, and average curves are shown as filled symbols with error bounds representing the standard error of the mean.

Atto655 conjugated secondary antibody. Superresolution imaging was accomplished using fluorescence localization microscopy by detecting mEos3.2 and Atto655 signals simultaneously under conditions that allowed for stochastic activation. Single molecules localized within at least 10,000 acquired images were used to reconstruct the representative superresolution images shown in Figure 2A.

Similarly to the diffraction-limited images of Figure 1C, pBCR staining in superresolved images indicates that activated BCRs are organized into extended clusters at the cell surface. In contrast, both PM and TM peptides appear as small puncta that are distributed more evenly across the cell surface. These tight puncta are most likely a consequence of observing the same

mEos3.2 fluorophore multiple times over the course of imaging. This overcounting effect is common to superresolution localization measurements and does not indicate that peptides are themselves organized into clusters (Veatch *et al.*, 2012; Stone *et al.*, 2017b). Cells were also imaged using interference contrast microscopy (ICM; Figure 2B). In these images, contrast arises from destructive interference between light reflected off the coverslip and membrane, with darker pixels indicating regions of closer contact (Weber, 2003). CH27 cells engaged with PC bilayers exhibit significant surface topography on their basal surfaces, with pBCR staining occurring largely at positions where the cell and supported membrane are in close contact (see insets of Figure 2B).

Codistributions of pBCR with minimal peptides are difficult to assess by eye due to incomplete spatial sampling and weak sorting of membrane peptides (Stone *et al.*, 2017b). Instead, images were quantified using pair cross-correlation functions, $g(r)$, tabulated from masked regions of cells as described in *Materials and Methods*. The cross-correlation function reports the density of localizations of one color probe a distance r from the average probe of the other color normalized to the average density of both probes in the region of interest. $g(r)$ is normalized so that values greater than 1 indicate co-clustering, values less than 1 indicate depletion, and values equal to 1 indicates a random codistribution within the specified error bounds. Figure 2C shows curves tabulated for individual cells, along with the average curve for each peptide. In principle, the magnitude of $g(r)$ is independent of the density of probes, beyond effects on signal to noise (Veatch *et al.*, 2012). We find that the magnitude of $g(r)$ is largely independent of the expression level of transiently expressed peptides (Supplemental Figure 2), indicating that peptides mark but do not significantly alter these membrane domains. In addition, the magnitude of pBCR binding is not greatly influenced by the expression levels of minimal peptide anchors (Supplemental Figure 3).

The cross-correlation functions in Figure 2C indicate that PM is enriched and TM is depleted from pBCR-labeled clusters engaged with PC bilayers. These curves are largely symmetric, with PM showing enrichment and TM showing depletion. The magnitude of the curves indicates that the average concentration of PM is roughly 30% higher within pBCR-labeled clusters than in the membrane overall, while the average concentration of TM is 30% lower in pBCR-labeled clusters than in the membrane overall. We note that the absolute magnitude of $g(r)$ is likely influenced by the significant membrane topography present in these samples, even though care was taken to exclude areas from the analysis where the membrane clearly traversed out of the TIR excitation field. Membrane topography on the order of the thickness of the excitation field (~100 nm) will lead to variation of observed membrane surface area and variation in the excitation intensity at the membrane, both of which will impact the apparent density of all membrane-bound components (Parmryd and Onfelt, 2013; Adler *et al.*, 2019). Our observation of depletion of the TM probe provides strong support for the conclusion that the observed heterogeneity is not dominated by topography effects, since these would tend to increase values of $g(r)$ at short displacements for all probe pairs.

Both TM and PM peptides lack protein interaction motifs; therefore, we conclude that their distribution is a consequence of their differential coupling to membrane phase-like domains. This observation for BCR engaged with its natural bilayer ligand is in good agreement with our past observations for BRCs engaged with soluble, artificial cross-linkers (Stone *et al.*, 2017a). Similar domains are not detected when cells are chemically fixed without receptor clustering (Stone *et al.*, 2017a), supporting the conclusion that receptor clustering acts to stabilize this domain.

Membrane domain partitioning is not sufficient to describe CD45 and Lyn partitioning with respect to bilayer-engaged BRCs

We next compared how the regulatory proteins CD45 and Lyn sort with respect to BRCs in order to estimate the extent to which membrane phase-like domains contribute to this organization. To accomplish this, we first modified the stimulation method to one with reduced membrane topography, which is needed to facilitate quantitative comparisons across experimental conditions (Figure 3). CH27 cells were prelabeled with biotin-atto655 Fab αIgM(μ)
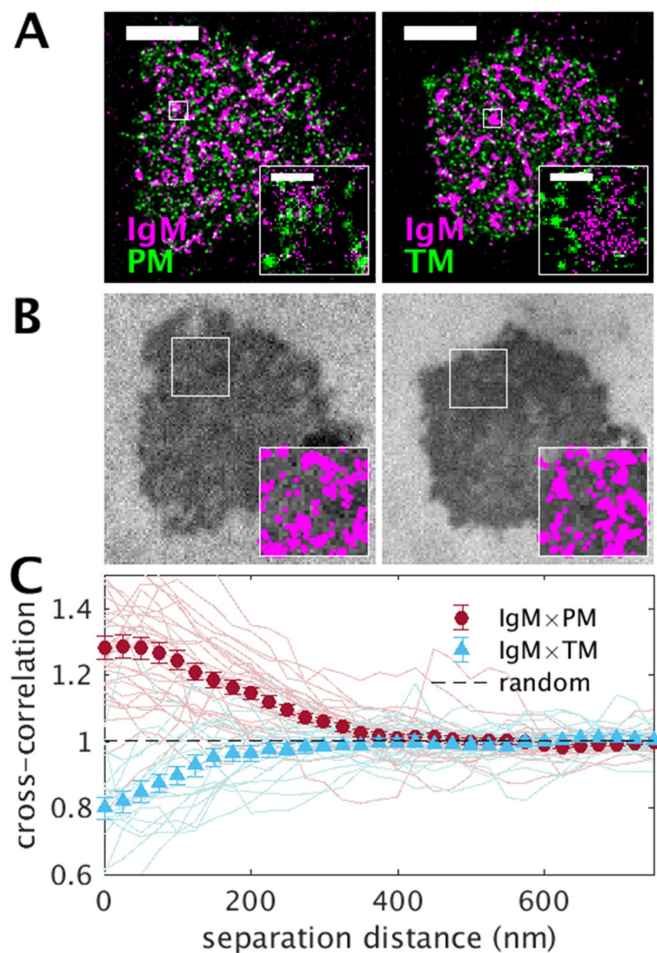

FIGURE 3: Cells engaged with bilayers through POPC and biotinylated Fab αIgM exhibit reduced basal surface topography and produce BRCs that sort minimal peptides. (A) Representative reconstructed superresolution images of BRCs, marked with biotinylated Fab αIgM conjugated to Atto655 and the minimal membrane anchored peptides PM (left) or TM (right) conjugated to mEos3.2. Cells were chemically fixed after 5 min of exposure to a POPC membrane presenting streptavidin, as described in *Materials and Methods*. Scale bars are 5 μm in main images and 500 nm in insets. (B) ICM images indicate that these cells exhibit reduced membrane topography across the basal cell surface as compared with the cells examined in Figure 2. Insets show that dark areas in the ICM image extend beyond clusters of pBCR localizations (magenta) from part A. (C) Cross-correlation functions tabulated for 31 cells between IgM and PM or 19 cells between IgM and TM from images acquired from at least three distinct sample preparations. Curves from individual cells are shown as lighter color lines and average curves are shown as filled symbols, with error bounds representing the standard error of the mean between cells.
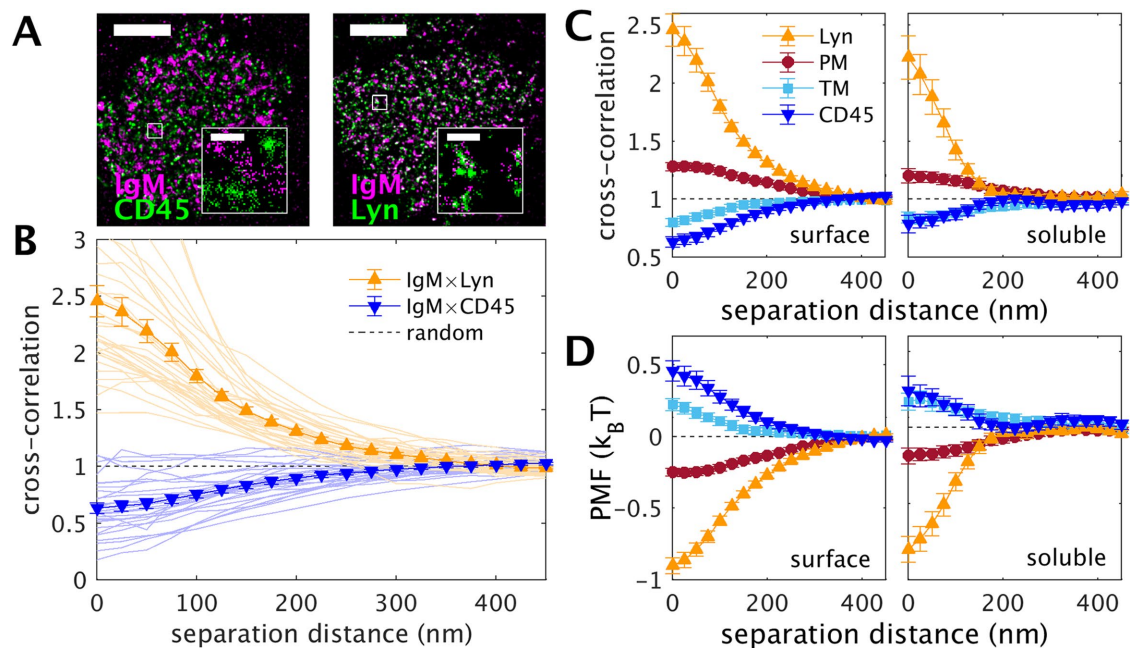
FIGURE 4: Full-length regulatory proteins sort with respect to BRCs. (A) Representative reconstructed superresolution images of BRCs, marked with biotinylated Fab αIgM conjugated to Atto655 and endogenously CD45 antibody labeled with Alexa 532 (left) or transiently expressed Lyn (right) conjugated to mEos3.2. Cells were chemically fixed after 5 min of exposure to a POPC membrane presenting streptavidin, as described in *Materials and Methods*. Scale bars are 5 μm in main images and 500 nm in insets. (B) Average cross-correlations between CD45 and Lyn with respect to IgM-BRCs tabulated from 28 and 32 cells, respectively, from images acquired from at least three distinct sample preparations. Curves from individual cells are shown as lighter color lines and average curves are shown as filled symbols, with error bounds representing the standard error of the mean between cells. (C) Left, Average cross-correlation curves from Figure 3C and panel B here plotted on the same axes to facilitate comparison. Right, Similar results obtained from measurements in which BCR marked with biotinylated Fab αIgM conjugated to Atto655 was clustered with soluble streptavidin. Representative images and individual curves for cells stimulated with soluble streptavidin are shown in Supplemental Figures 8 and 9. (D) Curves from part C replotted as the potential of mean force (PMF), where PMF(r) = $-k_BT$ ln($g(r)$).

and then engaged with a PC bilayer decorated with mobile strep-tavidin (Supplemental Figure 4). In these samples, BCR likely engages the membrane both through PC lipids and through biotinylated Fab αIgM, two interactions that can independently give rise to signaling through the BCR. This admittedly complex stimulus produces CH27 cells that exhibit markers of BCR activation (Supplemental Figure 5). BRCs marked by Fab αIgM are also sites of pBCR labeling, indicating that there is no significant pool of BCR that becomes activated by the PC bilayer away from αIgM clusters (Supplemental Figure 5).

Figure 3 shows the results from cells expressing PM and TM peptides prepared as described above for direct comparison with Figure 2. This stimulation condition produces larger BRCs that occupy more of the adhered cell surface than for CH27 cells stimulated through PC lipids alone (Supplemental Figure 6). Notably, ICM images indicate that these membranes lie flat on the supported membrane surface even at positions away from BRCs (Figure 3B). BRCs engaged via PC lipids and αIgM also sort phase-marking peptides in superresolved images (Figure 3C). Here, the magnitude of cross-correlation curves indicates that the average concentration of PM is roughly 30% higher within αIgM-labeled clusters than in the membrane overall, while the average concentration of TM is 20% lower in αIgM-labeled clusters than in the membrane as a whole. Again, codistribution of components is difficult to assess by eye, although subtle enrichment of PM and especially exclusion of TM from IgM BRCs is visually evident in reconstructed

superresolution images (insets in Figure 3A and additional cells in Supplemental Figures 7 and 8).

We next explored the sorting of CD45 and Lyn in BRCs engaged with bilayers as described above. Representative images of αIgM alongside endogenous CD45 or transiently expressed Lyn-meos3.2 are shown in Figure 4A. It is visually evident that CD45 is excluded from αIgM clusters, whereas Lyn is enriched, and this impression is verified in the quantifications over multiple cells shown in Figure 4B. Moreover, direct comparison of CD45 × IgM and TM × IgM cross-correlation functions in Figure 4C (left panel) indicates that CD45 is more robustly excluded from BRCs than TM, indicating that partitioning into membrane domains only partially determines the organization of this protein. The observed exclusion of CD45 is in good qualitative agreement with previously published diffraction-limited images of CD45 in B-cells stimulated by bilayer-presented ligands (Depoil *et al.*, 2008). This is in contrast to results obtained when BCR is cross-linked using a soluble streptavidin (Figure 4C, right panel), where the magnitude of CD45 exclusion with respect to BRCs is roughly equivalent to that of TM. Representative images and cross-correlation functions for cells stimulated with soluble streptavidin are shown in Supplemental Figures 9 and 10.

Correlation functions can be converted to the potential of mean force (PMF) through the relation PMF(r) = $-k_BT$ ln($g(r)$), where the PMF is the effective potential between the visualized components needed to give rise to the observed spatial codistribution at equilibrium (Veatch *et al.*, 2012). Curves representing the PMF

between BCR and CD45 or BCR and TM for both surface and soluble stimulation conditions are shown in Figure 4D. This analysis suggests that coupling to membrane domains provides roughly half of the energy required to describe CD45 exclusion (PMF($r < 25$ nm) = 0.22 ± 0.04 k_BT for αIgM × TM and 0.46 ± 0.07 k_BT for αIgM × CD45), while the remaining energy must come from other types of repulsive interactions in this system.

Lyn is more strongly recruited to BRCs than the ordered marker peptide PM when cells are engaged with either bilayer-presented or soluble streptavidin. This is expected, since Lyn is known to bind directly to phosphorylated BCR (Yamanashi *et al.*, 1991), so that its organization is partially dictated by this protein–protein interaction. Converting correlation functions to the PMF indicates that roughly ¼ of the energy required to describe the distribution of Lyn with respect to BRCs can be attributed to the partitioning of Lyn's membrane anchor into ordered domains. This is the case for both membrane-engaged BCR (PMF($r < 25$ nm) = -0.25 ± 0.03 k_BT for αIgM × PM and -0.90 ± 0.06 k_BT for αIgM × Lyn) and BCR engaged with the soluble streptavidin cross-linker (PMF($r < 25$ nm) = -0.18 ± 0.04 k_BT for αIgM × PM and -0.80 ± 0.08 k_BT for αIgM × Lyn).

pTyr localizes robustly with bilayer-engaged BRCs

Cells engaged with both soluble and bilayer-presented streptavidin stain with the generic pTyr antibody clone 4G10. This antibody binds to activated BCRs in addition to phosphorylated tyrosine sites on other cellular proteins. We conducted superresolution imaging measurements of IgM and pTyr in cells engaged with both bilayer-presented and soluble streptavidin, and results are summarized in Figure 5. In both cases, IgM and pTyr labels clearly colocalize in representative reconstructed images (Figure 5A), and colocalizion is apparent in the large amplitude of the cross-correlation functions tabulated between these two signals (Figure 5B).

A direct comparison of IgM × pTyr colocalization is complicated because the character of the IgM clusters formed varies dramatically between stimulation conditions. For example, the magnitude of the IgM × pTyr cross-correlation function is larger in the case of BCR clustering by soluble streptaviden ($g(r < 25$ nm) = 13.5 ± 1.1) than with BCR engagement with bilayer-presented streptavidin ($g(r < 25$ nm) = 4.7 ± 0.3). This difference arises largely from differences in the BRCs themselves, which yield dramatically different autocorrelations. Complete colocalization between pTyr and IgM would produce an IgM × pTyr cross-correlation function that as equivalent to the IgM × IgM autocorrelation function, minus contributions from overcounting individual IgM molecules. This is roughly what is observed 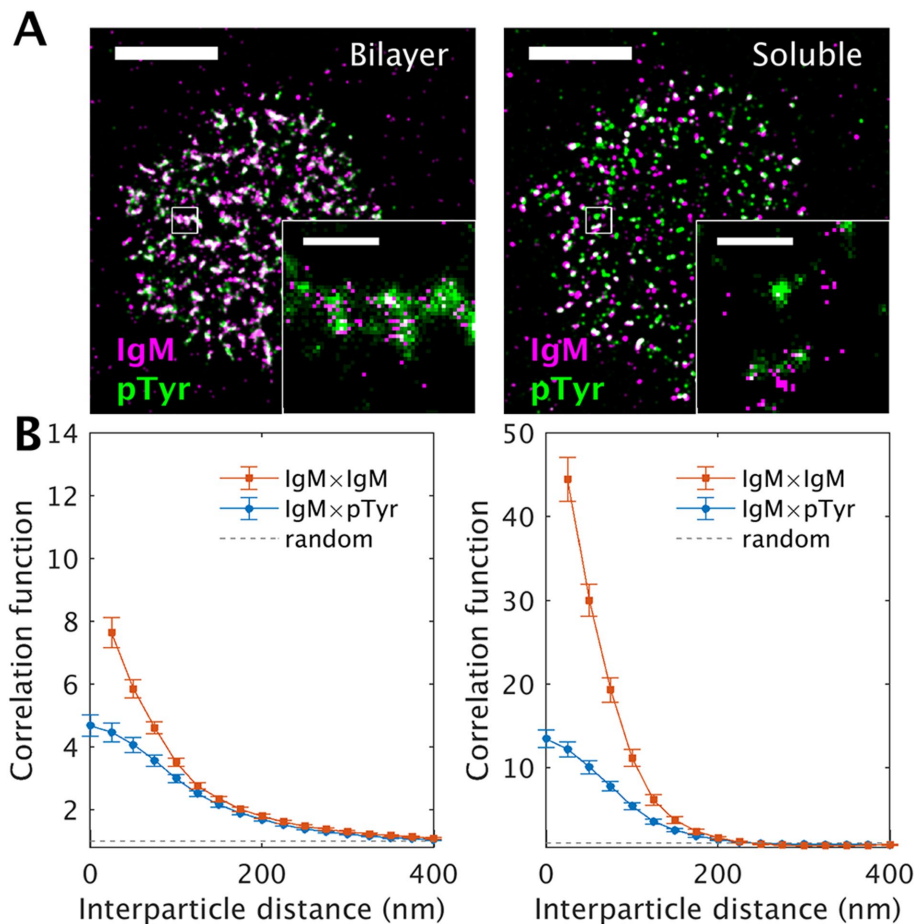for cells engaged with a bilayer, with cross-correlation and autocorrelation functions differing by less than a factor of 2 at short radii ($g(25$ nm $> r > 50$ nm) = 4.5 ± 0.3 for the cross-correlation vs. $g(25$ nm $> r > 50$ nm) = 7.7 ± 0.5 for the IgM autocorrelation; note that the autocorrelation is not calculated for $r < 25$ nm). The magnitude of the cross-correlation function is more dramatically reduced when compared with the autocorrelation in cells engaged with soluble streptavidin ($g(25$ nm $> r > 50$ nm) = 12.2 ± 0.9 vs. $g(25$ nm $> r > 50$ nm) = 44 ± 3), indicating that a fraction of the pTyr signal is detected away from IgM clusters under this stimulation condition. This observation is also evident in looking at the images themselves. For the most part, pTyr staining is not observed outside of IgM clusters for bilayer-engaged cells, but more pTyr signals are detected away from IgM clusters engaged with soluble streptavidin. Absolute densities of both IgM and pTyr are increased at the contact sites in cells engaged with streptavidin-presenting bilayers as compared with the ventral surfaces of cells stimulated with soluble streptavidin, as indicated by diffraction-limited imaging measurements (Supplemental Figure 11).

FIGURE 5: Tyrosine phosphorylation (pTyr) of artificially cross-linked IgM-BRCs. (A) Representative reconstructed superresolution images of Fab αIgM and total antibody-stained pTyr (clone 4G10) in CH27 cells engaged with bilayer-presented or soluble streptavidin for 5 min before fixation. Scale bars are 5 µm in main images and 500 nm in insets. (B) Average cross-correlation functions between IgM and pTyr contrasted with average autocorrelations for IgM for the two stimulation conditions shown in part A. Curves are tabulated from 33 cells with the bilayer cross-linker and 38 cells with the soluble cross-linker from images acquired from at least three distinct sample preparations. Error bounds represent the standard error of the mean between cells.

Membrane domains and phosphatase exclusion synergize collective receptor activation in a minimal model of early BRC signaling

In past work, we assembled a minimal model that produced collective receptor activation upon clustering within a heterogeneous membrane (Stone *et al.*, 2017a). Within this
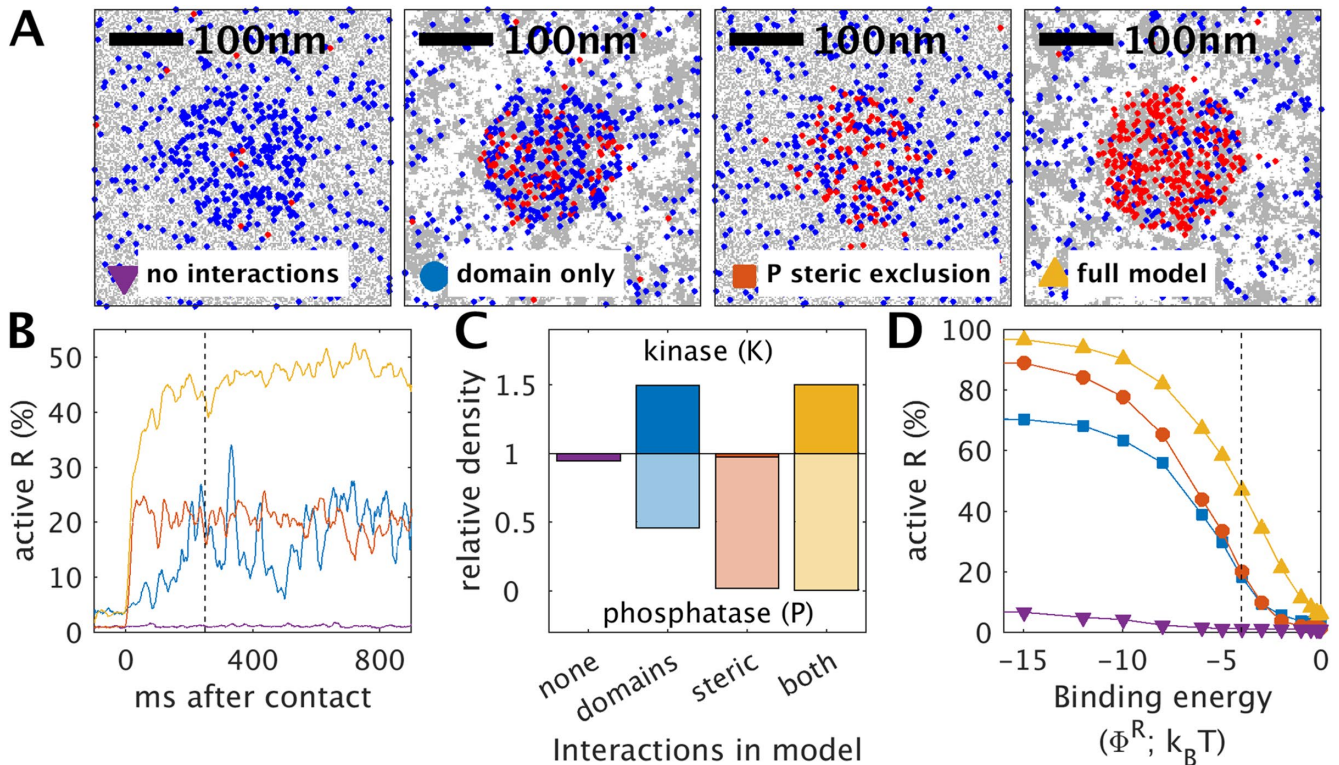
FIGURE 6: Simulations of a minimal model of receptor activation upon clustering. (A) Snapshots showing receptors and membrane domains taken from simulations of the four minimal models described in the main text. Gray and white pixels are ordered and disordered membrane regions, respectively. Receptors colored red are in an active state and receptors colored blue are in an inactive state. Receptors are clustered within a circle within the simulation frame through an applied field felt only by receptors and snapshots are generated from simulation results 250 ms after the application of this field. (B) Traces showing the average number of active receptors within the simulation frame as a function of time for the four models investigated. The dashed vertical line represents the time corresponding to the snapshots shown in A. (C) The relative concentration of kinase and phosphatase within the receptor cluster for each of the four models investigated. Concentration is normalized to the concentration of each component over the whole simulation frame. (D) Average receptor activation as a function of ligand affinity obtained by tuning the strength of the receptor clustering field Φ^R. Values are obtained by averaging values between 200 ms and 1 s after the application of the receptor clustering field. The dashed line indicates the receptor field strength corresponding to the snapshots shown in part A.

model, receptor clustering leads to the stabilization of an extended ordered membrane domain that enriches kinase and depletes phosphatase, based solely on their differential partitioning with membrane domains. Both receptors and kinase are represented as typical components that prefer ordered domains; phosphatases are represented as a typical component that prefers disordered domains. All proteins are embedded in a membrane that contains fluctuating domains and diffusive dynamics. Receptors are activated with low probability when they come into contact with a kinase and are deactivated with high probability when they come into contact with a phosphatase. Additionally, activated receptors have kinase activity to mimic kinase binding to phosphorylated receptors, inserting a positive feedback loop that enhances the signaling output. An equal number of phosphatase and kinase components are included for convenience, and parameters are chosen so that the receptor activation state is low (<5%) when receptors are not clustered in all models. A detailed description and justification of model parameters is included in *Materials and Methods*.

We have observed experimentally that membrane coupling alone is not sufficient to describe phosphatase exclusion from BRCs formed through interactions with a supported bilayer (Figure 4). To account for this, we have updated the model to include an additional direct repulsive interaction sensed only by the phosphatase within the receptor cluster. This direct repulsive interaction acts to reduce the local concentration of phosphatase within the receptor cluster, and for simplicity, we implemented a high potential to enforce complete exclusion of phosphatase.

In sum, four minimal models were interrogated. One contains no interactions other than the potential used to cluster receptors, while the remaining models probe systems with domains and with direct phosphatase exclusion individually and in combination. Representative simulation snapshots are shown in Figure 6A and several model outcomes are shown in Figure 6, B–D. We note that these models are not intended to replicate BCR signaling accurately, as this would require the inclusion of many different interaction partners and regulatory processes. Instead, we use the model to explore how the organizing principles of membrane domains and direct phosphatase exclusion could contribute to a clustering-mediated signaling process more generally.

We find that receptors collectively activate upon clustering in the three models including domains and/or direct exclusion of phosphatase, although the fraction of activated receptors varies between models. This is seen in the representative traces showing the percentage of receptors in an activated state (Figure 6B) taken from

the same simulations that produced representative snapshots (Figure 6A). In these examples, the full model has a large and sustained response, the direct phosphatase exclusion model has a sustained but reduced response, and the domain-only model responds, but the fraction of activated receptors varies more in time. The average activation levels can be understood by examining the relative concentrations of kinase and phosphatase within domains shown in Figure 6C. In the domain-only model, phosphatases can enter the receptor cluster, where they can deactivate many receptors, leading to a reduction in average activation and increased variability in average receptor activation over time. Receptors cannot be inactivated by phosphatase within receptor clusters in the models with direct phosphatase exclusion, leading to larger overall activated fractions and less variability within time. The difference in amplitude between the full model and the model with only phosphatase exclusion can be attributed to the local kinase concentrations in these models. Without domains, the local kinase concentration mimics that of the membrane as a whole, while domains facilitate the recruitment of kinase to receptor clusters, enhancing receptor activation. In addition, the number of receptors found in clusters is generally larger for the same clustering potential in models with domains. This is because coupling to domains makes receptor recruitment more cooperative, with receptors sensing an additional effective potential to localize with the other ordered components within this membrane region.

Figure 6D shows how receptor activation varies with affinity of the receptor-ligand binding association, which is tuned by varying the strength of the receptor clustering field (Φ^R). By this measure, the domain-only and direct phosphatase exclusion models yield roughly the same sensitivity, but vary in their maximum response under conditions of complete receptor clustering. To some extent, this agreement is due to parameters chosen for these examples, but it is meant to demonstrate that collective receptor activation upon clustering can occur via each of these mechanisms individually. Both sensitivity and the maximum stimulation capacity are enhanced in the model that combines membrane domains and direct phosphatase exclusion, demonstrating the potential synergy between these two distinct activation mechanisms.

DISCUSSION
BRCs engaged with lipid bilayers are larger and contain more receptors than those engaged with an artificial soluble cross-linker
Past work has demonstrated that BCR clustering is enhanced when receptors are engaged with surface-bound antigens via the participation of specific oligomerization motifs (Tolar et al., 2009a; Tolar and Pierce, 2010). Engaging BCR through mobile antigen on a fluid lipid bilayer has been shown to further enhance B-cell signaling, likely because active processes within cells can recruit BCRs to the contact site and gather BCR–antigen complexes into large domains (Pierce and Liu, 2010; Ketchum et al., 2014; Lee et al., 2017). In the current study, we made no attempt to present equivalent stimuli to cells engaged with soluble and bilayer-presented antigens, although measurements were conducted using a high concentration (or surface density) of streptavidin to ensure a robust response. Under the specific conditions we examine, receptor clusters are larger and contain more receptors when cells engage with lipid bilayers than when BCRs are clustered with an artificial soluble cross-linker (Supplemental Figures 6A and 11), likely due to the mechanisms described above.

Another important difference between BRCs engaged with soluble streptavidin and those engaged with bilayers is that the PC lipids used to form bilayers are also natural ligands for the BCRs expressed on CH27 cells (Figure 1), while soluble streptavidin clusters Fab antibodies bound to IgM BCR away from its natural ligand-binding site. Previous work indicates that engagement at the natural ligand-binding site can engage signaling mechanisms that are not engaged by artificial cross-linkers (Volkmann et al., 2016). Regardless of the mechanisms that give rise to the larger BRCs formed via bilayer stimulation, these structures provide a robust platform for investigating the sorting of plasma membrane proteins and peptides via superresolution fluorescence localization microscopy. BRCs in bilayer-engaged cells have characteristic length scales that exceed 100 nm on the average (Supplemental Figure 6A), which are well suited for imaging by this method, which typically resolves fluorophores with lateral resolution 20–30 nm.

Ordered domain stabilization is a general property of clustered IgM BCRs
This study quantifies the membrane composition proximal to BRCs established through interactions with planar lipid bilayers using multicolor superresolution fluorescence localization microscopy. We use lipids with PC headgroups as natural ligands to stimulate CH27 B-cells, and additionally engage BCRs through αIgM Fab, which binds to streptavidin presented on the bilayer. In both cases, BRCs enrich a peptide marker of the liquid-ordered phase (PM) and deplete a peptide marker of the liquid-disordered phase (TM), similarly to our previous observations in IgM BRCs engaged with soluble streptavidin (Stone et al., 2017a). This peptide sorting mimics that of these same peptide probes with respect to liquid-ordered domains in plasma membrane vesicles isolated from cells (Leventhal et al., 2010; Stone et al., 2017a), albeit on a smaller length scale and at a weaker magnitude. We refer to these BRCs as ordered, phase-like domains, and our observation of these domains under distinct stimulation conditions suggests that ordered domain stabilization is a unifying property of clustered IgM BCRs. These results add to an extensive past literature characterizing the IgM BCR microenvironment as an ordered membrane domain in a variety of experimental contexts (Cheng et al., 1999; Pierce, 2002, Sohn et al., 2006, 2008), as well as more recent studies describing heterogeneity in B-cell membranes (Gold and Reth, 2019).

Cross-correlation amplitudes cannot be compared directly across stimulation conditions
In the description of our experimental findings, we have intentionally avoided direct comparisons of correlation functions across stimulation conditions that produce dramatically different arrangements of BCRs. The complexity inherent in this type of comparison is demonstrated by the simulations shown in Figure 7. Here, a membrane contains circular domains that enrich a labeled component so that the density of labels within domains (ρ_{on}) is k_p times the density of labels outside of domains (ρ_{off}), where k_p is commonly referred to as the partition coefficient. In these examples, the magnitude of the cross-correlation function between the domains and the partitioning component is greater when membranes contain sparse domains than when membranes contain dense domains when k_p is held constant. Intuitively, this occurs because correlation functions are normalized to the average density of labels over the whole image (ρ_{ave}) rather than the average density of probes away from the domains. In this simplified two-state system, $\rho_{ave} = A\rho_{on} + (1 - A)\rho_{off}$, where A is the area fraction occupied by BRCs. The cross-correlation function at short displacements is roughly $g(r = 0) = \rho_{on}/\rho_{ave}$. Through algebraic manipulation,
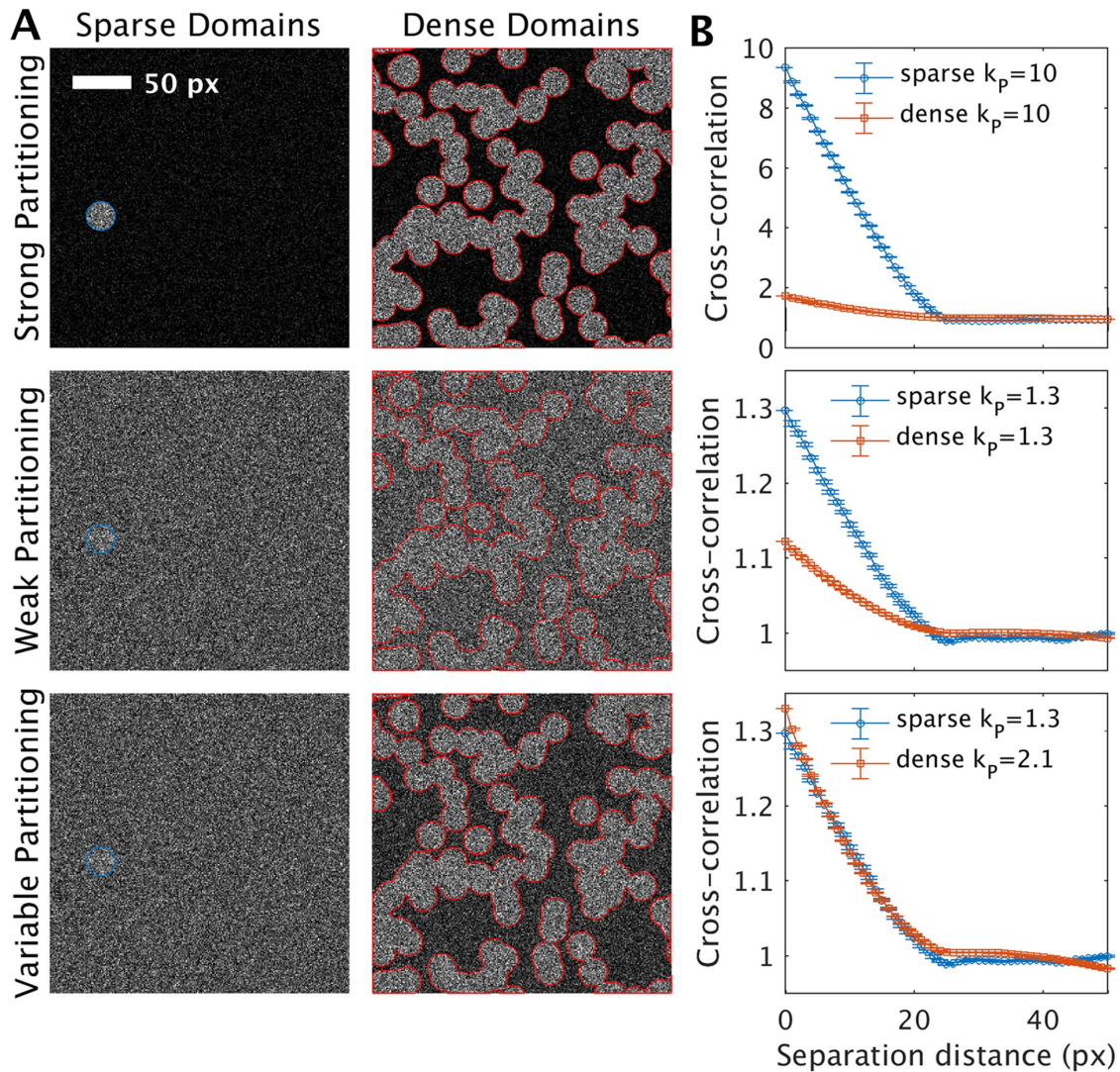
FIGURE 7: Correlation function amplitudes vary for simple partitioning when domains occupy different membrane area fractions. (A) Simulations of a simple domain-partitioning model where the density of probes within domains is k_P times the density of probes outside domains. Domains are randomly placed circles with radius 10 pixels (px). The density of probes within domains is held constant across simulations, as is the intensity range of displayed images. Domain edges are outlined in blue for sparse domains and red for dense domains and the same sparse and dense domain configuration is used in simulations with varying k_P. (B) Cross-correlation functions tabulated between the images from A and binary images of domains (unpublished data). For simulations with a single domain, the cross-correlation amplitude at $r = 0$ accurately reproduces the partition coefficient k_P. Top and middle panels, the cross-correlation amplitude is closer to 1 when many domains are present and k_P is held constant. Bottom panel, Matching cross-correlation function amplitudes for sparse and dense domains require that simulations be run with different k_P. k_P values indicated in legends correspond to those used to generate adjacent images.

$g(r = 0) = k_p/(1 - A(k_p - 1))$. When domains are sparse, the area fraction occupied by BRCs is small (A is close to zero), and $g(r = 0)$ is well approximated by k_p. When domains are dense, then A is no longer negligible and $g(r = 0)$ will trend closer to 1 for both enrichment ($k_p > 1$ and $g(r = 0) > 1$) and depletion ($k_p < 1$ and $0 < g(r = 0) < 1$). These trends can be seen in the curves shown in Figure 7B for probe enrichment within domains. This difference is most dramatic when k_p is far from 1 (top panels of Figure 7), but is still evident for weak partitioning (middle panels of Figure 7). The same correlation function amplitude can be maintained if k_p is enhanced for systems where domains occupy a larger fraction of the membrane surface (bottom panels of Figure 7).

In principle, this difference in domain density can be accounted for by comparing directly to the autocorrelation of each component, as is frequently done in fluorescence cross-correlation spectroscopy (Bacia et al., 2006). In practice, auto-correlation functions generated from superresolution localization microscopy images are inflated by the overcounting of single labeled molecules at short displacements while cross-correlation functions are not similarly impacted (Veatch et al., 2012). As a result, cross-correlation functions are always expected to have lower amplitudes than autocorrelation functions, especially at small displacements. The magnitude of this difference, even for the case of perfect localization, is difficult to estimate, as it depends on the absolute density of labeled molecules, which can

Ordered domains influence BCR signaling |

be difficult to estimate in superresolution localization measurements, especially when the component is highly organized (Veatch et al., 2012).

Phase-marking peptides partition more strongly with respect to bilayer-engaged IgM BRCs than to BRCs engaged with soluble antigens

We find that the cross-correlation amplitudes between IgM BCRs and the phase-marking probes PM and TM are roughly equivalent across stimulation conditions, even though the area fraction occupied by domains varies dramatically. As demonstrated in Figure 7, a constant correlation-function amplitude under these varying domain conditions indicates that the partition coefficient must also vary, with k_P farther from 1 for systems with a larger area fraction occupied by domains. This enhanced partitioning is subtly evident in reconstructed images themselves, especially in the case of TM exclusion (Figure 3 and Supplemental Figures 7 and 8). The robustness of partitioning is also evident when viewing the variation of cross-correlation functions obtained over an ensemble of single cells (compare Figures 2 and 3 with Supplemental Figure 9). This is in part because larger BRCs are better sampled in space by peptides, providing improved spatial statistics of peptide localizations both within and outside of BRCs.

In Figure 4, $g(r < 25 \text{ nm})$ is roughly 0.8 for BCR $\times$ TM and 1.3 for BCR $\times$ PM. If we assume that the area fraction taken up by clusters is $A = 1/4$, then k_P becomes 0.75 for TM and 1.4 for PM. If $A = 1/2$, then k_P becomes 0.67 for TM and 1.86 for PM. These k_P values are within the range found for similar peptides with respect to phase-separated domains in isolated GPMVs (Diaz-Rohrer et al., 2014) and stabilized phase-like domains in vesicles adhered to supported membranes (Zhao et al., 2013). In this study, we have not attempted to measure A, the area fraction occupied by BRCs, although it varies significantly from cell to cell and over the stimulation modes investigated.

What might be the cause of this enhanced partitioning? As discussed above, BRCs under the two stimulation conditions are fundamentally different, as is the effective stimulus. Bilayer-engaged BRCs are larger, contain more receptors, and likely contain more and possibly different proteins that act downstream of initial receptor activation. BRCs engaged with surfaces could also be further depleted of proteins that partition with disordered domains, such as observed for CD45. These factors could combine to more strongly favor ordered phase-like domains under this stimulation condition.

We consistently observe that the characteristic length scale of correlations between BCR and PM is larger than the characteristic length scale of anticorrelation between BCR and TM (Supplemental Figure 6). This observation could be a consequence of membrane topography, which would be expected to increase correlations over a length scale set by this topography (Parmryd and Onfelt, 2013). It is more exciting to speculate that the difference in the range of peptide recruitment and exclusion from BRCs reflects hierarchical organization of BCR microclusters, which contain scaffolding elements, numerous signaling regulators, recycling machinery, and cytoskeleton. It is possible that the peptides used in this study as markers of ordered and disordered membrane domains also sense other aspects of microclusters, such as membrane curvature or electrostatics.

Tyrosine phosphorylation activity is localized to receptor clusters in bilayer-engaged cells

Lyn and phosphatases such as CD45 are involved in regulating early stages of BCR tyrosine phosphorylation, as well as the pTyr state of scaffolding elements and other signaling regulators within the BCR activation pathway. For this reason, it is expected that pTyr levels are enhanced and pTyr proteins colocalize with BRCs in cells stimulated with both surface-presented and soluble antigens. Cells engaged with bilayer-presented streptavidin form BRCs that are larger and contain more receptors than cells engaged with soluble streptavidin; therefore it is likely that these clusters contain more possible pTyr sites. This effect alone may give rise to the elevated pTyr staining in bilayer-engaged BCRs as compared with BCRs cross-linked with soluble streptavidin that is observed in this study (Supplemental Figure 11). It is also possible that the enhanced depletion of CD45 and potentially other phosphatases also contributes to this effect for bilayer-engaged cells. Additional experiments would be necessary to distinguish these possibilities clearly.

Interestingly, we also observed surprisingly low pTyr levels away from BRCs formed via interactions with bilayer-presented versus soluble cross-linkers. This is seen in the images and quantification of Figure 5. It is possible that this occurs because the phosphatase concentration away from BRCs is elevated under the condition of a bilayer-presented cross-linker. It is tempting to speculate that changes in membrane protein and lipid composition away from receptors themselves contribute to signaling outcomes.

Phase-like domains can work in concert with other sorting mechanisms to organize signaling regulators

In the current study, we identify that CD45 is more excluded from BRCs than can be attributed to its transmembrane anchor for the case of bilayer-engaged BCRs, indicating that other organizing principles must contribute to its membrane organization. We have not identified the mechanism of this direct exclusion, but it likely arises from features of its extracellular and/or cytoplasmic domains.

CD45 and other phosphatases implicated in regulating BCR signaling, such as CD148 (Kishihara et al., 1993; Byth et al., 1996; Harwood and Batista, 2009), have large extracellular domains. Past studies in other cell types have demonstrated that proteins with large extracellular domains can be excluded from regions of tight engagement between receptors and a ligand-presenting membrane (Harwood and Batista, 2008, Zhu et al., 2008). For the case of transmembrane phosphatases, this local exclusion from regions of receptor engagement with ligands is referred to as the kinetic segregation model (Davis and van der Merwe, 2006) and has been tested directly in the context of T-cell receptor signaling (Cordoba et al., 2013; Razvag et al., 2018). Direct studies to test this model have not been reported for BCR signaling. In our studies with labeled CD45, the majority of receptors are likely tethered via a Fab and streptavidin linker, itself quite large, and may reduce CD45 exclusion via a kinetic segregation mechanism.

Studies using reconstituted cytoplasmic domains of CD45 tethered to supported membranes through histidine tags and nickel-chelating lipids find that this truncated protein is excluded from domains rich in other truncated and membrane-tethered proteins within the TCR signaling system (Su et al., 2016). This suggests that CD45 can be excluded from membrane regions rich in prostimulatory proteins based solely on properties of its cytoplasmic domain. The direct exclusion observed in the current study for bilayer-engaged BCRs could arise from this type of interaction. We do not observe evidence for direct exclusion of CD45 from BRCs engaged with soluble streptavidin. This may indicate that cytoplasmic regions differ dramatically between the two stimulation methods, or that the direct exclusion observed in this study is dominated by interactions arising from the extracellular domain as described above.

Lyn kinase is implicated in the initial tyrosine phosphorylation of BCR that is required to recruit the soluble kinase Syk and other signaling elements to BRCs (Yamanashi *et al.,* 1991, Kurosaki *et al.,* 1995; Porto Dal *et al.,* 2004). We observe that the anchor sequence PM provides only part of the energy required to describe Lyn recruitment to BRCs, which is expected because full-length Lyn is known to bind to phosphorylated BCR (Yamanashi *et al.,* 1991). We attribute the enhanced Lyn localization with BRCs to these direct protein-binding events. In our minimal model of receptor clustering, this enhanced kinase recruitment is not incorporated explicitly, but occurs indirectly, because activated receptors have kinase activity. Within the model, we envision that the majority of receptor-bound kinases represent soluble kinases such as Syk, but could also include some quantity of Lyn.

In general, receptors lack tyrosine phosphorylation when the effective activity of the phosphatase outpaces that of the kinase, and will tend to become phosphorylated when either kinase activity increases or phosphatase activity decreases. Past work using reconstituted elements of the T-cell receptor system has demonstrated that this biochemical network is highly sensitive to small changes in in the concentrations of these key regulators (Hui and Vale, 2014). The simulations presented in Figure 6 mimic the key aspect of the kinetic segregation model by including a repulsive interaction at sites of receptor engagement felt only by phosphatases. As described by others (Davis and van der Merwe, 2006; Choudhuri *et al.,* 2009; Schmid *et al.,* 2016; Junghans *et al.,* 2018; Fernandes *et al.,* 2019), we find that this mechanism alone is capable of inducing receptor activation upon engagement by lowering the concentration and therefore the activity of phosphatase.

Our simulations additionally demonstrate that the sensitivity and dynamic range of this signaling system is enhanced when it is also coupled to membrane domains. Membrane domains facilitate this enhancement through several avenues. First, local kinase concentration is increased at sites of receptor engagement, enabling receptor activation with higher phosphatase concentrations or more robust activation at the same phosphatase levels. Domains also facilitate collective recruitment of receptors to sites of ligand engagement, increasing the avidity of the ligand–receptor interaction. This occurs because ligand binding compensates for the losses in mixing entropy accrued by confining a receptor to the cluster in an otherwise uniform membrane. When membrane domains are present, the free energy cost of organizing receptors is lowered, and thus less binding energy is required to recruit the same number of receptors. A true experimental test of this model would require that experiments be conducted with an equivalent stimulus (represented in the model as the receptor-clustering field, Φ^R), which was not attempted in the current study. Nonetheless, the model demonstrates how combining these distinct mechanisms could enhance the versatility of this signaling system, which is reactive to a broad range of stimuli.

Summary and concluding remarks

In this study, we have shown that BRCs sort minimal markers of ordered and disordered phases when CH27 cells are engaged with bilayers of PC lipids, a natural ligand for the BCRs expressed in this cell line. This result, combined with past observations, supports the idea that ordered domain stabilization is a general feature of BCR activation that likely contributes to signaling functions. We show that phase-like domain partitioning is not sufficient to describe CD45 exclusion from bilayer-engaged BCR, in contrast to observations with an artificial soluble BCR cross-linker. This indicates that additional interactions contribute to the organization of this protein

for bilayer engaged BCRs, although this study does not identify the source of this direct interaction. Simulations of a minimal model that combines direct phosphatase exclusion with coupling to membrane domains demonstrates the synergy of these distinct organizing principles, enhancing the sensitivity and dynamic range of this signaling system. Overall, this work supports the concept that the BCR signaling system is versatile and can draw from a variety of different protein–protein and protein–lipid interactions to tune sensitivity to a broad range of stimuli.

MATERIALS AND METHODS
Cell culture

CH27 mouse B-cells (Millipore Cat# SCC115, RRID: CVCL_7178), a lymphoma-derived cell line (Haughton *et al.,* 1986), were acquired from Neetu Gupta (Cleveland Clinic). Cells were maintained in culture as previously described (Stone and Veatch, 2015). Prior to measurements, cells are typically pelleted from media by spinning at $500 \times g$ for 5 min and resuspended into a live cell–compatible minimal buffer consisting of 15.0 mM NaCl, 5.0 mM KCl, 1.8 mM $CaCl_2$, 1.0 mM $MgCl_2$, 6.0 mM glucose, and 20 mM HEPES, pH 7.4.

Large unilamellar vesicle formation

Lipids, suspended in chloroform, were dried to form a thin film under N_2 while being vortexed in a clean glass tube. The lipid film was then placed under vacuum for 30 min to remove any residual solvent and then hydrated in either purified water or phosphate-buffered saline (PBS). In some cases, the resulting multilamellar vesicles (MLVs) were subjected to 10 freeze–thaw cycles. Large unilamellar vesicles (LUVs) were obtained by extruding the MLVs 31 times with a miniextruder (Avanti, 610000) using 10 mm–diameter filters (Whatman Drain Disc, 230300) and a membrane of pore size 0.1 μm (Whatman Nucleopore Track-Etched Membrane, 800309). The final concentration of lipid in LUV suspensions was either 3 or 1 mg/ml. LUVs were stored at 4°C and used within 2 wk.

Flow chamber and supported planar lipid bilayer assembly

Flow chambers were assembled from a 25 × 75 × 1–mm plain microscope slide (Fisherbrand, 12-550D) and a clean No. 1.5 22 × 22–mm glass coverslip (Fisherbrand, 12-541B) on the day of the experiment. Coverslips were cleaned through rinsing with water, ethanol, and then chloroform before drying under N_2. In some cases, coverslips were acid–cleaned in NoChromix (Sigma-Aldrich Cat# 328693). The microscope slide and coverslip were plasma–cleaned for 5 min (Harrick Plasma, PDC-32G). Two 1 × 2.5–cm strips of PARAFILM were cut and placed on the middle of the microscope slide with 1 cm of space between them. The coverslip was placed on top of the PARAFILM, and the entire flow chamber was placed on a hot plate at 100°C until the PARAFILM melted and sealed the slide and coverslip together. PBS was introduced to prime the chamber prior to lipid deposition.

Planar lipid bilayers were fused from LUVs hydrated in purified water. LUV mixture (50 μl) was diluted 1:1 in PBS, introduced to the flow chamber and incubated at room temperature for 30 min, and then washed with PBS and incubated for 1 h at room temperature to allow the bilayer to equilibrate. For measurements involving bilayer-presented streptavidin cross-linkers, 0.5 mol% biotinyl-DOPE (Avanti, 870273C) was included in the LUV preparation. Following bilayer assembly, membranes were incubated for 10 min with 200 μl of a 1–μg/ml streptavidin solution at room temperature. Prior to incubation with cells, all bilayers were rinsed in the live cell–compatible buffer.

Supported lipid bilayers were also prepared on glass-bottomed Mattek Petri dishes that were cleaned with ethanol, dried, and then plasma-cleaned before incubation with LUV solution diluted in PBS. After incubation, samples were washed. Care was taken that the lipid film was not exposed directly to air.

Calcium mobilization assays

CH27 cells were loaded with 2 µg/ml Fluo-4AM (Invitrogen: F14201) for 5 min at room temperature in 1 ml T/B/S buffer (15.0 mM NaCl, 5.0 mM KCl, 1.8 mM $CaCl_2$, 1.0 mM $MgCl_2$, 6.0 mM glucose, 20 mM HEPES, 1 mg/ml bovine serum albumin [BSA], 0.25 mM sulfinpyrazone, pH 7.4). The cell suspension was subsequently diluted to a final volume of 15 ml with T/B/S buffer and incubated for 30 min at 37°C to allow dye loading. After the 30-min incubation, the cells were spun down at $500 \times g$ for 5 min and resuspended in 3 ml of T/B/S buffer.

For IgM BCR engagement with streptavidin cross-linkers, Fuo-4AM loaded cells were additionally incubated with Fab-biotin anti-mouse IgM (Jackson ImmunoResearch Labs Cat# 115-067-020, RRID: AB_2338587) for 10 min at 37°C. Cells were pelleted and resuspended in T/B/S buffer before measurements.

For microscope measurements of calcium mobilization, cells loaded with Fluo-4 were introduced into a Mattek well placed on an inverted microscope stage and imaged over time with 10× magnification. At the early time points, cells were seen to settle into the focal field, so the number of cells detected varied as a function of time. For soluble stimulation with dimeric antibody fragments (f(Ab)₂) αIgM, the soluble antibody was added directly to a Mattek well containing adhered cells. Fluorescence detection of Fluo-4 intensity was accomplished using an incoherent LED light source centered at 488 nm (pE excitation system; Cool LED, Andover UK), a quad band filter cube (LF405/488/561/647; Coherent), and an EMCCD camera (iXon-897; Andor, South Windsor, CT). Images were acquired over 10 min for each sample with an integration time of 0.5 s. Quantification of Fluo-4 intensity within cell boundaries was accomplished from images through an automatic watershed segmentation algorithm in Matlab to obtain the average response over the field of cells. Traces were normalized to the final value for cases where the signal appeared to fall back to the baseline. When possible, traces were normalized to the initial value before stimulation. Traces in figures are from single experiments but are representative of results obtained over at least three independent measurements.

For measurements of calcium mobilization in suspension, 100,000 cells per well loaded with Fluo-4 were placed in a 96-well plate and imaged with a microplate plate reader (SpectraMax iD33; Molecular Devices, San Jose, California). LUVs (25 µl) were added to 175 µl of cells at time 0 so that the final concentration of lipid was 12.5 µg/ml. Temperature was held at 30°C for all samples to ensure that the POPE LUVs would be in a liquid state. Fluorescence intensity was measured at 0.5-s increments for 10 min. Raw fluorescence intensity was normalized by the values detected <5 s after the injection, before the detected rise in fluorescence emission intensity. Traces shown represent the average values of normalized curves over at least three independent measurements and shaded regions represent the SD between measurements

Fluorophore and biotin conjugation to secondary antibodies

Biotinylation and Atto555 conjugation of goat Fab anti-mouse IgM (Jackson ImmunoResearch Labs Cat# 115-007-020, RRID:AB_2338477) were accomplished simultaneously. Amine-reactive biotin-X (2.25 µl, 15 mM), SE (Invitrogen: B1582), and NHS-Ester Atto655 (0.45 µl, 10 mM, Millipore-Sigma: 76245) were mixed with

the Fab (150 µl, 1.3 mg/ml, pH 8.5) and rotated for 1 h at room temperature in an aqueous solution buffered by 0.01M NaH_2PO_4 with 0.01M NaH_2CO_3. After incubation, the modified Fab was purified and separated from unbound dye through a gel filtration column (GE Healthcare Illustra NAP Columns from Fisher: 45-000-151) in 1X-PBS+1 mM-EDTA. The modified antibody was further purified by centrifugation in a Vivaspin-500 polyethersulfone concentration spin column with a 30-kDa cutoff (Vivaspin: VS0121). The modified antibody was then conjugated a second time to additional NHS-ester Atto655 by mixing 0.4 µl of 10 mM of the NHS-ester Atto655 with the modified antibody at room temperature at pH 8.5 for 1 h. The antibody was purified through the gel column and spin column again before its optical spectrum was obtained to estimate degree of label (~3 dye/antibody).

Biotinylation and silicon rhodamine (SiR) conjugation of goat Fab anti-mouse IgM was accomplished similarly. Amine-reactive biotin-X (3.5 µl, 15 mM), SE (Invitrogen: B1582), and NHS-ester SiR (2.0 µl, 10 mM, Spirochrome: SC003) were mixed with the Fab (300 µl, 1.3 mg/ml, pH 8.5) and rotated for 1 h at room temperature in an aqueous solution buffered by 0.01 M NaH_2PO_4 with 0.01 M NaH_2CO_3. After incubation, the modified Fab was purified as described above.

In some cases, secondary antibodies were fluorescently labeled following similar procedures, but the amine-reactive biotin-X was left out of the reaction mixture.

DNA constructs and transient transfection

The plasmids used for this study were described previously (Stone *et al.*, 2017a). Briefly, Lyn-eGFP and PM-eGFP plasmids (Pyenta *et al.*, 2001) were gifts from Barbra Baird and David Holowka (Cornell University, Ithaca, NY) and were cloned using standard techniques to replace eGFP with mEos3.2. Plasmid DNA encoding mEos3.2 protein and YFP-TM were gifts from Akira Ono (University of Michigan, Ann Arbor, MI). The YFP-TM plasmid encodes the transmembrane domain of LAT (linker for activation of T-cells) fused to the YFP so that the fluorescent protein was on the extracellular side of the cell. This plasmid was cloned using standard techniques to replace YFP with mEos3.2. The mEos3.2–tagged constructs used here are in a Clontech N1 plasmid vector background (Clontech, Mountain View, CA).

CH27 cells were transiently transfected by Lonza Nucleofector electroporation (Lonza, Basel, Switzerland) with electroporation program CA-137. Typically, 10^6 CH27 cells were transfected with 1.0 µg of plasmid DNA. For measurements involving stimulation at surfaces, transfected cells were grown overnight in a T-25 cell culture flask with filter caps in 5 ml of growth medium. The following day, the transfected cells were harvested and pelleted at $500 \times g$ for 5 min before being labeled for sample preparation. For measurements involving stimulation with soluble cross-linkers, transfected cells were grown overnight on glass-bottom Mattek Petri dishes for next-day sample preparation.

Preparation of samples for fluorescence microscopy

For stimulation by PC membranes, unlabeled live CH27 cells were suspended in live cell–compatible minimal buffer at room temperature (15.0 mM NaCl, 5.0 mM KCl, 1.8 mM $CaCl_2$, 1.0 mM $MgCl_2$, 6.0 mM glucose, 20 mM HEPES, pH 7.4) and then introduced into a flow chamber presenting a PC-containing membrane. Cells were incubated for 5 min before chemical fixation in 2% paraformaldehyde (PFA), 0.15% glutaraldehyde in 0.5X PBS for 20 min. Fixation was quenched by incubating with PBS containing 3% BSA for 20 min at room temperature.

For stimulation of CH27 cells by bilayer-presented streptavidin on PC membranes, live CH27 cells in suspension were pelleted at

500 × g for 5 min at 4°C and then incubated on ice for 10 min with 5 µg/ml anti-IgM Fab modified with biotin and Atto655 in the live cell–compatible buffer defined above. Cells were washed twice through centrifugation at 500 × g for 5 min at 4°C and ultimately suspended in room-temperature buffer. Cells were then introduced into a flow chamber containing a streptavidin-loaded bilayer and incubated for 5 min in the live cell–compatible buffer at room temperature before chemical fixation.

For BCR labeling and stimulation using soluble streptavidin, CH27 cells were incubated overnight in a Mattek well to facilitate their natural adhesion to glass. Cells were then labeled in 5 µg/ml anti IgM Fab modified with biotin and Atto655 in the live cell–compatible buffer for 10 min at room temperature. Cells were rinsed in the live cell–compatible buffer before incubation with streptavidin (1.0 µg/ml) for 5 min, followed by chemical fixation.

For cells engaged with surface-bound transferrin, 2 mg/ml biotinylated BSA was incubated with a clean flow chamber for 10 min at room temperature. After washing, flow cells were incubated with 1 µg/ml streptavidin solution for 10 min at room temperature. Live CH27 cells in suspension were pelleted at 500 × g for 5 min at 4°C and then incubated on ice for 10 min with 3.5 µg/ml biotinylated transferrin (Sigma-Aldrich: T3915) in the live cell–compatible buffer. Cells were washed twice through centrifugation at 500 × g for 5 min at 4°C and ultimately suspended in room-temperature live cell–compatible buffer before being loaded into the flow chamber, where they were allowed to adhere for 5 min before chemical fixation.

For phosphorylated BCR (pBCR) detection, chemically fixed cells were permeabilized in 0.1% Triton X-100 and then labeled with anti-human phosphotyrosine CD79A (Tyr182) rabbit antibody (Cell Signaling Technology Cat# 5173, RRID: AB_10694763). The primary antibody was detected using one of two secondary goat anti-rabbit polyclonal antibodies. A commercially labeled Alexa 532 secondary was used (Invitrogen: A-11009) for diffraction-limited images and for images acquired alongside IgM. For superresolution measurements alongside transiently expressed peptides, an unlabeled secondary antibody (Jackson ImmunoResearch Labs Cat# 111-005-003, RRID:AB_2337913) was conjugated to Atto655 using methods described above.

For phosphotyrosine (pTyr) detection, chemically fixed and permeabilized cells were labeled with anti-phosphotyrosine 4G10 Platinum mouse monoclonal antibody of the IgG2b subclass (Millipore Cat# 05-1050, RRID: AB_916371). The primary antibody was detected using a secondary goat anti-mouse IgG Fcγ subclass 2b antibody (Jackson ImmunoResearch Labs Cat# 115-005-207, RRID: AB_2338463). The secondary antibody was conjugated to Alexa Fluor 532 using methods described above.

For CD45 detection, chemically fixed CH27 B-cells were incubated with anti-mouse CD45R (B220) primary antibody clone RA3-6B2 conjugated directly to Alexa 532 (Thermo Fisher Scientific Cat# 14-0452-81, RRID: AB_467253).

Imaging

Imaging was performed using an Olympus IX81-XDC inverted microscope. TIRF laser angles where achieved using a cellTIRF module, a 100X UAPO TIRF objective (NA = 1.49), and active Z-drift correction (ZDC; Olympus America) as described previously (Stone and Veatch, 2014, 2015; Stone et al., 2017a). Atto 655 and SiR were excited using a 647-nm solid state laser (OBIS, 100 mW, Coherent) and Alexa 532 was excited using a 532-nm diode-pumped solid state laser (Samba 532–150 CW, Cobolt). Photoactivation of mEos3.2 was accomplished with a 405-nm diode laser (CUBE 405-50FP, Coherent) and it was simultaneously excited with a 561-nm

solid state laser (Sapphire 561 LP, Coherent). Simultaneous imaging of Atto655 or SiR and mEos3.2 was accomplished using a LF405/488/561/647 quadband filter cube (TRF89902, Chroma, Bellows Falls, VT), while imaging of Atto655 or Sir and Alexa532 was accomplished using a 405/488/532/647 quadband filter cube (Chroma, Bellows Falls, VT). Emission was split into two channels using a DV2 emission splitting system (Photometrics) with a T640lpxr dichroic mirror to separate emission: ET605/52m to filter near-red emission, and ET700/75m to filter far-red emission (Chroma).

Diffraction-limited images were acquired by maintaining laser intensities and TIR illumination angles to enable comparison of intensities observed across samples. Cells within individual images were masked by hand, and pixel values within the mask were used to obtain average values.

Interference contrast microscopy (ICM) images were acquired by illuminating samples with a broad-band incoherent light source centered at 565 nm (pE excitation system; Cool LED, Andover UK). Collected light was filtered using a U-C QUAD T2 cube (TIRF C155405, Chroma, Bellows Falls, VT).

Superresolution localization microscopy images were obtained by adjusting laser intensities so that single fluorophores could be distinguished in individual frames, and were generally between 5 and 20 kW/cm². Integration times were maintained at 20 ms and at least 10,000 individual images were acquired per cell. Samples labeled with BCR-Atto 655 and mEos3.2 were imaged in a buffer found to be optimal for fluorescence localization microscopy with these probes: 30 mM Tris, 9 mg/ml glucose, 100 mM NaCl, 5 mM KCl, 1 mM KCl, 1 mM MgCl₂, 1.8 mM CaCl₂, 10 mM glutathione, 8 µg/ml catalase, and 100 µg/ml glucose oxidase, pH 8.5 (Stone et al., 2017a). Samples labeled with Atto 655 and Alexa 532 were imaged in a buffer more suitable for the inorganic dye pair (Heilemann et al., 2009): 50 mM Tris, 100 mg/ml glucose, 10 mM NaCl, 100 mM 2-mercaptoethanol, 50 µg/ml glucose oxidase, and 200 µg/ml catalase, pH 8. Samples labeled with SiR and Alexa532 were imaged in 50 mM Tris, 100 mg/ml glucose, 10 mM NaCl, 100 mM 2-mercaptoethanol, 10 µg/ml glucose oxidase, and 200 µg/ml catalase, pH 8.5.

Single-molecule localization and superresolution image reconstruction

Candidate finding for single-molecule fitting was accomplished by fitting the intensity profile of local maxima in background-subtracted and wavelet-filtered images using two-dimensional Gaussian functions as described previously (Stone et al., 2017a). Once candidates were fitted and localized, they were culled to remove outliers based on size, intensity, and localization error for each color using software described previously (Veatch et al., 2012). The near-red channel was overlaid onto the far-red channel using an image transform matrix calculated from fiducial bead-marker images obtained during each experiment. The images were aligned to account for stage drift, which resulted in the final reconstructed STORM image from the culled, transformed, and aligned localizations. Final image resolution and the surface density of probes were calculated for each color using previously described methods (Veatch et al., 2012).

Localizations used to generate reconstructed images are grouped so that probes detected in sequential image frames within a specified radius are averaged to single localizations. Reconstructed images shown in the figures were generated from a two-dimensional histogram of grouped localizations with pixels of 25 nm. In the main images, histograms were filtered with a two-dimensional Gaussian function with SD 50 nm, which is greater than the resolution of the

image, which is typically 20–30 nm. Insets within images are histogram images drawn without filtering.

Correlation analysis

Autocorrelation and cross-correlation functions were tabulated from masked, reconstructed superresolution images using previously described methods (Sengupta et al., 2011; Veatch et al., 2012; Stone et al., 2017a). Images were reconstructed with 25-nm pixels from ungrouped localizations for cross-correlations and from grouped images for autocorrelations, and in both cases, images were not filtered before correlation functions were tabulated. Average cross-correlation functions were obtained through a simple average over single-cell measurements, and errors presented on average curves represent the standard error of the mean. In the figures, the numbers of cells used to generate average correlation functions are included in the captions. In all cases, these images sample from at least three independent experimental preparations.

Simulations of receptor activation

A conserved–order parameter two-dimensional Ising model was simulated on a 256 × 256 square lattice (~65,000 pixels) as described previously (Machta et al., 2011; Burns et al., 2016; Stone et al., 2017a) with minor modifications. Briefly, components that prefer ordered or disordered regions are represented as pixels that have value of $S = +1$ and $S = -1$, respectively, and an equal number of +1 and −1 components were included in all simulations. The vast majority of +1 and −1 pixels represent patches of unspecified membrane components representing proteins and lipids. In addition, 200 pixels with values of +1 are classified as receptors, 100 pixels with values of +1 are classified as kinases, and 100 pixels with values of −1 are classified as phosphatases. Receptors are clustered by applying an attractive circular field (φ^R) at the center of the simulation frame that only acts on receptors. In some simulations, a repulsive field with the same dimensions as φ^R is applied that only acts on phosphatases (φ^P). The final Hamiltonian is given by

$$H = -\sum_{i,j} S_i S_j + \sum_i R_i \Phi_i^R + \sum_i P_i \Phi_i^P$$

The first term sums over the four nearest neighbors (j) surrounding the pixel i and applies to all components. The second term contributes only when receptors occupy position i, where $R_i = 1$, and otherwise $R_i = 0$. The third term contributes only when phosphatases occupy position i, where $P_i = 1$, and otherwise $P_i = 0$. The fields Φ_i^R and Φ_i^R have a circular shape with a radius of 48 pixels (~100 nm; ~7000 pixels) centered in a simulation box with periodic boundary conditions.

Components are moved around the simulation box using a Monte Carlo algorithm that maintains detailed balance. Energy is calculated for proposed moves, and moves are accepted stochastically with probability exp(–β∆H), where β is the inverse temperature (T) multiplied by Boltzmann's constant (k_B) and ∆H is the change in energy between initial and final states. Simulations were run at either $1.1T_C$, for models with membrane domains, or $10T_C$, for models without membrane domains, where $T_C = 2/\ln(1+\text{sqrt}(2))$ is the critical temperature of the two-dimensional Ising model. The receptor and phosphatase fields are made independent of the temperature of the membrane by multiplying by T/T_C so that the acceptance probability of moves into and out of the field does not vary with β. The magnitude of the receptor field is varied between −0.01 and −100 $k_B T/T_C$, filling the range from weak to complete receptor clustering. The magnitude of the phosphatase field was held constant at +10 $k_B T/T_C$, a value that results in complete phosphatase depletion.

If a move is accepted that places a receptor next to a kinase, then the receptor is phosphorylated at a low probability (0.15%). If a move is accepted that places a receptor next to a phosphatase, then the receptor is dephosphorylated at a high probability (100%). Changes in phosphorylation state do not satisfy detailed balance. These parameter choices result in a low level of receptor activation before receptor clustering (<5%). When receptors are activated, they gain kinase activity, in that a move that places an activated receptor next to a second receptor results in the second receptor becoming phosphorylated at a low probability (0.15%). In this simple model, tuning parameters of protein concentration and reaction rates produce roughly equivalent results (e.g., doubling the efficiency of kinase is roughly equivalent to doubling kinase concentration). Similar results are anticipated for simulations where the number of phosphatases greatly exceeds the number of kinase components and reactions are accomplished at the same probability, or when parameters are tuned to intermediate levels of asymmetry in reaction probabilities and protein concentrations.

All simulations were initially run using nonlocal exchanges to decrease equilibration times. After equilibration, exchanges were then restricted to nearest neighbors in order to mimic diffusive dynamics. Simulation sweeps were converted to time assuming a diffusion coefficient of roughly 4 μm²/s, with one sweep corresponding to roughly 1 μs. Simulations were recorded for 10^6 sweeps, which corresponds to roughly 1 s, and configurations were saved every 1000 sweeps, corresponding to 1 ms.

Simulations of probe partitioning

Domains were generated by randomly placing circles of radius 10 pixels on a 256 × 256 square lattice. The probe images were generated by randomly incrementing pixels in order to maintain the partition coefficient indicated. In all cases, the average intensity within domains (ρ_{in}) was held constant at 5/pixel, while the density away from domains (ρ_{out}) varied according to $k_P = \rho_{in}/\rho_{out}$. Cross-correlation functions were tabulated between images of domains and probes with periodic boundary conditions.

All analyses were carried out in MATLAB (MATLAB, RRID: SCR_001622).

REFERENCES

Adler J, Sintorn IM, Strand R, Parmryd I (2019). Conventional analysis of movement on non-flat surfaces like the plasma membrane makes Brownian motion appear anomalous. Commun Biol 2, 12.

Albersdorfer A, Feder T, Sackmann E (1997). Adhesion-induced domain formation by interplay of long-range repulsion and short-range attraction force: a model membrane study. Biophys J 73, 245–257.

Bacia K, Kim SA, Schwille P (2006). Fluorescence cross-correlation spectroscopy in living cells. Nat Methods 3, 83–89.

Bakalar MH, Joffe AM, Schmid EM, Son S, Podolski M, Fletcher DA (2018). Size-dependent segregation controls macrophage phagocytosis of antibody opsonized targets. Cell 174, 131–142.e113.

Batista FD, Iber D, Neuberger MS (2001). B cells acquire antigen from target cells after synapse formation. Nature 411, 489–494.

Betzig E, Patterson GH, Sougrat R, Lindwasser OW, Olenych S, Bonifacino JS, Davidson MW, Lippincott-Schwartz J, Hess HF (2006). Imaging intracellular fluorescent proteins at nanometer resolution. Science 313, 1642–1645.

Burns MC, Nouri M, Veatch SL (2016). Spot size variation FCS in simulations of the 2D Ising model. J Phys D Appl Phys 49, 214001.

Byth KF, Conroy LA, Howlett S, Smith AJ, May J, Alexander DR, Holmes N (1996). CD45-null transgenic mice reveal a positive regulatory role for CD45 in early thymocyte development, in the selection of CD4+CD8+ thymocytes, and B cell maturation. J Exp Med 183, 1707–1718.

Carbone CB, Kern N, Fernandes RA, Hui E, Su X, Garcia KC, Vale RD (2017). In vitro reconstitution of T cell receptor-mediated segregation of the CD45 phosphatase. Proc Natl Acad Sci USA 114, E9338–E9345.

Carrasco YR, Batista FD (2006). B-cell activation by membrane-bound antigens is facilitated by the interaction of VLA-4 with VCAM-1. EMBO J 25, 889–899.

Carrasco YR, Fleire SJ, Cameron T, Dustin ML, Batista FD (2004). LFA-1/ICAM-1 interaction lowers the threshold of B cell activation by facilitating B cell adhesion and synapse formation. Immunity 20, 589–599.

Cheng PC, Cherukuri A, Dykstra M, Malapati S, Sproul T, Chen MR, Pierce SK (2001). Floating the raft hypothesis: the roles of lipid rafts in B cell antigen receptor function. Semin Immunol 13, 107–114.

Cheng PC, Dykstra ML, Mitchell RN, Pierce SK (1999). A role for lipid rafts in B cell antigen receptor signaling and antigen targeting. J Exp Med 190, 1549–1560.

Choudhuri K, Parker M, Milicic A, Cole DK, Shaw MK, Sewell AK, Stewart-Jones G, Dong T, Gould KG, van der Merwe PA (2009). Peptide-major histocompatibility complex dimensions control proximal kinase-phosphatase balance during T cell activation. J Biol Chem 284, 26096–26105.

Choudhuri K, Wiseman D, Brown MH, Gould K, van der Merwe PA (2005). T-cell receptor triggering is critically dependent on the dimensions of its peptide-MHC ligand. Nature 436, 578–582.

Cordoba SP, Choudhuri K, Zhang H, Bridge M, Basat AB, Dustin ML, van der Merwe PA (2013). The large ectodomains of CD45 and CD148 regulate their segregation from and inhibition of ligated T-cell receptor. Blood 121, 4295–4302.

Davis SJ, van der Merwe PA (2006). The kinetic-segregation model: TCR triggering and beyond. Nat Immunol 7, 803–809.

Depoil D, Fleire S, Treanor BL, Weber M, Harwood NE, Marchbank KL, Tybulewicz VL, Batista FD (2008). CD19 is essential for B cell activation by promoting B cell receptor-antigen microcluster formation in response to membrane-bound ligand. Nat Immunol 9, 63–72.

Diaz-Rohrer BB, Leventar KR, Simons K, Leventar I (2014). Membrane raft association is a determinant of plasma membrane localization. Proc Natl Acad Sci USA 111, 8500–8505.

DiLillo DJ, Horikawa M, Tedder TF (2011). B-lymphocyte effector functions in health and disease. Immunol Res 49, 281–292.

Fernandes RA, Ganzinger KA, Tzou JC, Jonsson P, Lee SF, Palayret M, Santos AM, Carr AR, Ponjavic A, Chang VT, et al. (2019). A cell topography-based mechanism for ligand discrimination by the T cell receptor. Proc Natl Acad Sci USA 116, 14002–14010.

Fleire SJ, Goldman JP, Carrasco YR, Weber M, Bray D, Batista FD (2006). B cell ligand discrimination through a spreading and contraction response. Science 312, 738–741.

Freeman SA, Goyette J, Furuya W, Woods EC, Bertozzi CR, Bergmeier W, Hinz B, van der Merwe PA, Das R, Grinstein S (2016). Integrins form an expanding diffusional barrier that coordinates phagocytosis. Cell 164, 128–140.

Gold MR, Reth MG (2019). Antigen Receptor function in the context of the nanoscale organization of the B cell membrane. Annu Rev Immunol 37, 97–123.

Harwood NE, Batista FD (2008). New insights into the early molecular events underlying B cell activation. Immunity 28, 609–619.

Harwood NE, Batista FD (2009). Early events in B cell activation. Annu Rev Immunol 28, 185–210.

Haughton G, Arnold LW, Bishop GA, Mercolino TJ (1986). The CH series of murine B cell lymphomas: neoplastic analogues of Ly-1+ normal B cells. Immunol Rev 93, 35–51.

Heilemann M, van de Linde S, Mukherjee A, Sauer M (2009). Super-resolution imaging with small organic fluorophores. Angew Chem Int Ed Engl 48, 6903–6908.

Hess ST, Girirajan TP, Mason MD (2006). Ultra-high resolution imaging by fluorescence photoactivation localization microscopy. Biophys J 91, 4258–4272.

Howard M, Paul WE (1983). Regulation of B-cell growth and differentiation by soluble factors. Annu Rev Immunol 1, 307–327.

Hui E, Vale RD (2014). In vitro membrane reconstitution of the T-cell receptor proximal signaling network. Nat Struct Mol Biol 21, 133–142.

Junghans V, Santos AM, Lui Y, Davis SJ, Jonsson P (2018). Dimensions and interactions of large T-cell surface proteins. Front Immunol 9, 2215.

Ketchum C, Miller H, Song W, Upadhyaya A (2014). Ligand mobility regulates B cell receptor clustering and signaling activation. Biophys J 106, 26–36.

Kishihara K, Penninger J, Wallace VA, Kundig TM, Kawai K, Wakeham A, Timms E, Pfeffer K, Ohashi PS, Thomas ML, et al. (1993). Normal B lymphocyte development but impaired T cell maturation in CD45-exon6 protein tyrosine phosphatase-deficient mice. Cell 74, 143–156.

Kurosaki T, Johnson SA, Pao L, Sada K, Yamamura H, Cambier JC (1995). Role of the Syk autophosphorylation site and SH2 domains in B cell antigen receptor signaling. J Exp Med 182, 1815–1823.

Kurosaki T, Shinohara H, Baba Y (2009). B cell signaling and fate decision. Annu Rev Immunol 28, 21–55.

LeBien TW, Tedder TF (2008). B lymphocytes: how they develop and function. Blood 112, 1570–1580.

Lee J, Sengupta P, Brzostowski J, Lippincott-Schwartz J, Pierce SK (2017). The nanoscale spatial organization of B-cell receptors on immunoglobulin M- and G-expressing human B-cells. Mol Biol Cell 28, 511–523.

Leventar I, Lingwood D, Grzybek M, Coskun U, Simons K (2010). Palmitoylation regulates raft affinity for the majority of integral raft proteins. Proc Natl Acad Sci USA 107, 22050–22054.

Lingwood D, Simons K (2010). Lipid rafts as a membrane-organizing principle. Science 327, 46–50.

Lorent JH, Diaz-Rohrer B, Lin X, Spring K, Gorfe AA, Leventar KR, Leventar I (2017). Structural determinants and functional consequences of protein affinity for membrane rafts. Nat Commun 8, 1219.

Machta BB, Papanikolaou S, Sethna JP, Veatch SL (2011). Minimal model of plasma membrane heterogeneity requires coupling cortical actin to criticality. Biophys J 100, 1668–1677.

Mercolino TJ, Arnold LW, Haughton G (1986). Phosphatidyl choline is recognized by a series of Ly-1+ murine B cell lymphomas specific for erythrocyte membranes. J Exp Med 163, 155–165.

Minguet S, Dopfer E-P, Schamel WW (2010). Low-valency, but not monovalent, antigens trigger the B-cell antigen receptor (BCR). Int Immunol 22, 205–212.

Monroe JG, Dorshkind K (2007). Fate decisions regulating bone marrow and peripheral B lymphocyte development. Adv Immunol 95, 1–50.

Niiro H, Clark EA (2002). Decision making in the immune system: regulation of B-cell fate by antigen-receptor signals. Nat Rev Immunol 2, 945.

Parmryd I, Onfelt B (2013). Consequences of membrane topography. FEBS J 280, 2775–2784.

Pierce SK (2002). Lipid rafts and B-cell activation. Nat Rev Immunol 2, 96–105.

Pierce SK, Liu W (2010). The tipping points in the initiation of B cell signalling: how small changes make big differences. Nat Rev Immunol 10, 767–777.

Porto Dal, MJ, Gauld SB, Merrell KT, Mills D, Pugh-Bernard AE, Cambier J (2004). B cell antigen receptor signaling 101. Mol Immunol 41, 599–613.

Pyenta PS, Holowka D, Baird B (2001). Cross-correlation analysis of inner-leaflet-anchored green fluorescent protein co-redistributed with IgE receptors and outer leaflet lipid raft components. Biophys J 80, 2120–2132.

Razvag Y, Neve-Oz Y, Sajman J, Reches M, Sherman E (2018). Nanoscale kinetic segregation of TCR and CD45 in engaged microvilli facilitates early T cell activation. Nat Commun 9, 732.

Reth M (1992). Antigen receptors on B lymphocytes. Annu Rev Immunol 10, 97–121.

Rey-Suarez I, Wheatley B, Koo P, Bhanja A, Shu Z, Mochrie S, Song W, Shroff H, Upadhyaya A (2020). WASP family proteins regulate the mobility of the B cell receptor during signaling activation. Nat Comm 11, 439.

Rust MJ, Bates M, Zhuang X (2006). Sub-diffraction-limit imaging by stochastic optical reconstruction microscopy (STORM). Nat Methods 3, 793–795.

Sackmann E, Smith AS (2014). Physics of cell adhesion: some lessons from cell-mimetic systems. Soft Matter 10, 1644–1659.

Schmid EM, Bakalar MH, Choudhuri K, Weichsel J, Ann HS, Geissler PL, Dustin ML, Fletcher DA (2016). Size-dependent protein segregation at membrane interfaces. Nat Phys 12, 704–711.

Sengupta P, Jovanovic-Talisman T, Skoko D, Renz M, Veatch SL, Lippincott-Schwartz J (2011). Probing protein heterogeneity in the plasma membrane using PALM and pair correlation analysis. Nat Methods 8, 969–975.

Sieckmann DG, Asofsky R, Mosier DE, Zitron IM, Paul WE (1978). Activation of mouse lymphocytes by anti-immunoglobulin. I. Parameters of the proliferative response. J Exp Med 147, 814–829.

Simons K, Ikonen E (1997). Functional rafts in cell membranes. Nature 387, 569–572.

Sohn HW, Tolar P, Jin T, Pierce SK (2006). Fluorescence resonance energy transfer in living cells reveals dynamic membrane changes in the initiation of B cell signaling. Proc Natl Acad Sci USA 103, 8143–8148.

Sohn HW, Tolar P, Pierce SK (2008). Membrane heterogeneities in the formation of B cell receptor-Lyn kinase microclusters and the immune synapse. J Cell Biol 182, 367–379.

Stone MB, Shelby SA, Núñez MF, Wisser K, Veatch SL (2017a). Protein sorting by lipid phase-like domains supports emergent signaling function in B lymphocyte plasma membranes. Elife 6, e19891.

Stone MB, Shelby SA, Veatch SL (2017b). Super-resolution microscopy: shedding light on the cellular plasma membrane. Chem Rev 117, 7457–7477.

Stone MB, Veatch SL (2014). Far-red organic fluorophores contain a fluorescent impurity. ChemPhysChem 15, 2240–2246.

Stone MB, Veatch SL (2015). Steady-state cross-correlations for live two-colour super-resolution localization data sets. Nat Commun 6, 7347.

Su X, Ditlev JA, Hui E, Xing W, Banjade S, Okrut J, King DS, Taunton J, Rosen MK, Vale RD (2016). Phase separation of signaling molecules promotes T cell receptor signal transduction. Science 352, 595–599.

Tolar P, Hanna J, Krueger PD, Pierce SK (2009a). The constant region of the membrane immunoglobulin mediates B cell-receptor clustering and signaling in response to membrane antigens. Immunity 30, 44–55.

Tolar P, Pierce SK (2010). A conformation-induced oligomerization model for B cell receptor microclustering and signaling. Curr Top Microbiol Immunol 340, 155–169.

Tolar P, Sohn HW, Liu W, Pierce SK (2009b). The molecular assembly and organization of signaling active B-cell receptor oligomers. Immunol Rev 232, 34–41.

Veatch SL, Machta BB, Shelby SA, Chiang EN, Holowka DA, Baird BA (2012). Correlation functions quantify super-resolution images and estimate apparent clustering due to over-counting. PLoS One 7, e31457.

Volkmann C, Brings N, Becker M, Hobeika E, Yang J, Reth M (2016). Molecular requirements of the B-cell antigen receptor for sensing monovalent antigens. EMBO J 35, 2371–2381.

Weber I (2003). Reflection interference contrast microscopy. Methods Enzymol 361, 34–47.

Woodruff MF, Reid B, James K (1967). Effect of antilymphocytic antibody and antibody fragments on human lymphocytes in vitro. Nature 215, 591–594.

Yamanashi Y, Kakiuchi T, Mizuguchi J, Yamamoto T, Toyoshima K (1991). Association of B cell antigen receptor with protein tyrosine kinase Lyn. Science 251, 192–194.

Youinou P (2007). B cell conducts the lymphocyte orchestra. J Autoimmun 28, 143–151.

Zhao J, Wu J, Veatch SL (2013). Adhesion stabilizes robust lipid heterogeneity in supercritical membranes at physiological temperature. Biophys J 104, 825–834.

Zhu JW, Brdicka T, Katsumoto TR, Lin J, Weiss A (2008). Structurally distinct phosphatases CD45 and CD148 both regulate B cell and macrophage immunoreceptor signaling. Immunity 28, 183–196.